Neutron Dark-Field Tomography

M. Strobl,[1,2] C. Grünzweig,[3] A. Hilger,[2] I. Manke,[2] N. Kardjilov,[2] C. David,[3] and F. Pfeiffer[3,4]

[1]*University of Heidelberg, Im Neuenheimer Feld 253, 69120 Heidelberg, Germany*
[2]*Helmholtz Zentrum Berlin, Glienickerstrasse 100, 14109 Berlin, Germany*
[3]*Paul Scherrer Institut, 5232 Villigen PSI, Switzerland*
[4]*Ecole Polytechnique Fédérale de Lausanne, 1015 Lausanne, Switzerland*

(Received 4 May 2008; revised manuscript received 9 July 2008; published 15 September 2008)

We report how a grating interferometer yields neutron dark-field scatter images for tomographic investigations. The image contrast is based on ultrasmall-angle scattering. It provides otherwise inaccessible spatially resolved information about the distribution of micrometer and submicrometer sized structural formations. Three complementary sets of tomographic data corresponding to attenuation, differential phase, and small-angle scattering can be obtained from one measurement. The method is compatible with conventional imaging and provides significantly higher efficiency than existing techniques.

DOI: 10.1103/PhysRevLett.101.123902 PACS numbers: 42.30.Wb, 03.75.Dg, 28.20.Cz, 42.25.Fx

Neutron imaging as well as x-ray imaging has recently experienced the development of a broad variety of methods [1–26], like phase contrast [1–6], differential phase contrast [1,7–15], and dark-field imaging [16–21], to name a few. Although such methods are well established and routinely used with x-rays, not all methods could be implemented for neutrons straightforwardly, due to the different nature of neutron radiation compared to electromagnetic waves. Even more impeding is the fact that a number of methods, even when successfully realized, cannot achieve comparable impact, because the inherently limited available phase space density of neutron beams compared to state-of-the-art light sources hinders an efficient application. This applies especially when techniques require high spatial and chromatic coherence (concerning $\Delta\lambda/\lambda$), since the necessary beam conditioning implies dramatic flux losses. The implementation of a grating interferometer in a conventional transmission imaging setup marked a milestone in the development of neutron phase-contrast imaging and tomography [14]. The superiority of the grating interferometer technique is owed to relaxed coherence requirements concerning both spatial and chromatic coherence. These conditions enable even quantitative phase-contrast tomography on reasonable time scales despite the low available phase space density of neutron beams. The setup, first developed for low-brilliance x-ray sources [9,10] could successfully be adapted to neutrons, taking into account the quantum optical properties of these matter waves of massive particles [14].

The grating-based shearing interferometer as shown in Fig. 1 consists of a source grating G0, a phase grating G1, and an analyzer absorption grating G2 [27]. The absorption source grating with a period p_0 provides a partially coherent beam for the phase grating G1 inducing a phase shift of π with a period of p_1. The analyzer grating with a period $p_2 = p_1/2$ at the 1st fractional Talbot distance enables the detection of the interference pattern despite a detector resolution more than an order of magnitude too low to resolve the period of the intensity oscillations. To resolve the fringe pattern a phase stepping approach is applied by recording several images for different scan positions of, e.g., the analyzer grating. The grating periods are chosen

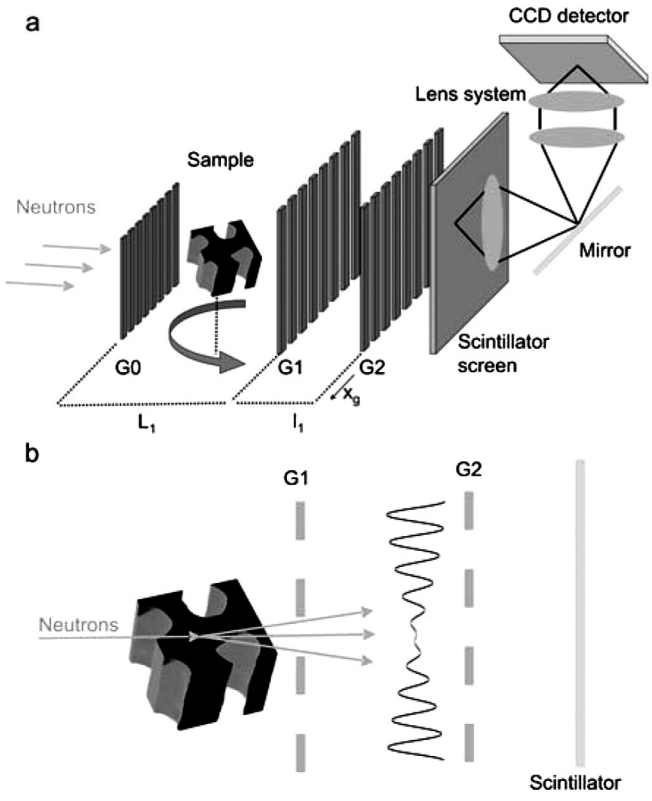

FIG. 1. Grating interferometer. (a) Setup with three gratings, sample, and detector system. (b) The interference pattern induced by grating G1 smeared due to scattering in the sample.

according to the condition $p_0 = p_2 L_1/l_1$ with respect to the distance L_1 between source and phase grating and l_1, the 1st fractional Talbot distance depending on the used neutron wavelength λ. Such parameters guarantee for a constructive superposition of the interference patterns of beams originating from different lines of the source grating. The number and width of lines in the source grating define the available flux on the sample and only the total illuminated width D of G0 together with the distances L from G0 to the object and l from object to detector defines the achievable spatial resolution through the geometric blur $d = lD/L$ of the setup. Hence, spatial and angular resolution are decoupled and consequently differential phase effects can be detected in spite of relaxed coherence conditions. Analyzing the phase shifts of the fringes and the mean intensity over one fringe period for a tomographic measurement provides volumetric reconstructions of the real and the imaginary part of the refractive index distribution [14]. The results are comparable to such achieved in perfect double crystal diffractometers; however, the exposure times necessary with this method are approximately 2 orders of magnitude shorter for comparable spatial resolution [28].

The fundamental idea of the approach presented in this Letter is to exploit another parameter for tomography in analogy to results achieved in a double crystal setup with neutrons [21] by taking advantage of the grating interferometer. As described in detail in Ref. [21], in contrast to differential phase effects, scattering to very small angles does not cause a shift directed to one direction, but a broadening of the angular intensity distribution. This broadening is of the order of arc-seconds and can be detected and exploited for x-ray and neutron imaging with perfect crystals [17–19,21]. Consequently it causes also a spatial broadening of the maxima of the fringe pattern in the grating interferometer, which has a comparable angular resolution. Indeed the broadening of the maxima at constant periodic positions reduces the visibility of the fringe pattern. Hence, the spatially resolved relative visibility, i.e., the variation of the local amplitude of the fringe pattern is—as described in Refs. [19,20]—a scattering related imaging parameter analogue to dark-field imaging or ultrasmall-angle scattering contrast. The high efficiency of this technique enables an expansion of the field of applications to three-dimensional tomographic investigations, provided that a tomographic reconstruction method is available for this parameter.

The description of the local increase of the angular width B of a beam due to (ultra) small-angle scattering [21] along a straight path in the y direction through the sample,

$$B(x) = \sqrt{\int_{\text{path}} f_B(x, y)dy} = \sqrt{\int_{\text{path}} \frac{\sigma(x, y)N(x, y)}{R^2(x, y)}dy}, \quad (1)$$

assumes multiple scattering [29] and a Gaussian distribution. The generalized scattering parameter f_B is defined by the local scattering cross section $\sigma(x, y)$, the scattering particle density $N(x, y)$, the product of which defines the reciprocal mean free path length, and a radius $R(x, y)$ denoting a correlation length, respectively, an average size parameter of the scattering structure. The Radon transformation—the basis of a tomographic reconstruction—can be written as the projection functions

$$P_\theta(t) = B_\theta^2(t) = \int f_B(x, y(x, \theta, t))\delta_D(t - x\cos\theta - y\cos\theta)dxdy \quad (2)$$

where δ_D is the Dirac delta function. The coordinate transformation providing the lateral position $t = (x\cos\theta + y\sin\theta)$ at a projection angle θ is accounting for the tomography geometry. Consequently, when the broadening of the angular distribution due to scattering can be measured, the sample can be reconstructed in terms of the generalized scattering parameter f_B. However, the grating interferometer provides a sinusoidal response, in contrast to an approximately Gaussian distribution in a diffractometer. The intensity oscillations $I(x_g)$ in a detector pixel for a scan of the analyzer grating along the traverse direction x_g can be written in a Fourier series

$$I(x_g) = \sum_i a_i \cos(ikx_g + b_i) \approx a_0 + a_1 \cos(kx_g + b_1) \quad (3)$$

involving the amplitude and phase coefficients a_i and b_i and $k = 2\pi/p_2$. Because of the scattering the oscillations are smeared corresponding to a convolution of $I(x_g)$ with the scattering function approximated by a Gaussian with the width B. Analogous to the loss of modulation transfer for a broader point spread function the visibility given by the ratio of amplitude a_1 and offset a_0 decreases with increasing B. Consequently the scattering function can be analyzed through the width of the point spread function and extracted as long as the visibility does not disappear completely. As a result, the recorded spatially resolved oscillation patterns provide, in addition to the previously exploited parameters—differential phase (b_1) and attenuation (a_0)—also the oscillation amplitude (a_1) as an imaging parameter.

The experiments have been performed at the Berlin Neutron Scattering Center (BENSC) using the cold neutron imaging instrument CONRAD [30]. A double crystal device [23] was enabled to choose a wavelength $\lambda = 0.35$ nm ($\Delta\lambda/\lambda \sim 5\%$ [28]) coinciding with the maximum of the spectrum provided by the corresponding neutron guide NL1b. The source grating has been placed right behind the monochromator device with its lines directed vertically. Such geometry defines the horizontal plane for angular resolution of the setup. The distance L_1 from source grating G0 to the phase grating G1 was 4.5 m. The corresponding periods have been $p_0 = 791$ μm, $p_1 = 7.96$ μm, and $p_2 = 4$ μm. The distance l_1 between G1

and G2 was 22.74 mm. A cross section of app. 30×30 mm^2 of the source grating G0 and the full cross sections of the gratings G1 and G2 of 64×64 mm^2 have been illuminated. The images were recorded with a state-of-the-art scintillator-CCD detector. The scintillator was a 200 μm thick silver doped LiF/ZnS screen. Via a mirror the scintillation light was recorded by a CCD camera (ANDOR DV434) with an optical lens system (Nikkor 50 mm). The scintillator screen was mounted a few millimeters behind the analyzer grating, and according to $L = 4.47$ m, $D = 3$ cm, and $l = 5$ cm, a final spatial resolution of about 180 μm was achieved. Exposure times for single images have been up to 2 min and 9 images have been recorded in order to scan the intensity oscillation in the course of phase stepping.

Figure 2 shows the experimental results of a radiographic phase stepping measurement obtained for a reference test sample made of Al. In Figs. 2(a) and 2(b) the processed conventional attenuation image (a_0), respectively, the differential phase image (b_1) are shown. The dark-field image (a_1/a_0) is displayed in Fig. 2(c). Despite the relatively low attenuation coefficient of Al ($\mu \sim 0.1$ cm^{-1}) the conventional attenuation image [Fig. 2(a)] yields reasonable contrast for the bulk sample. However, the differential phase image is superior providing better definition of the edges of the sample especially regarding the cylindrical holes which display enhanced contrast (visible as well-defined vertical lines) [Fig. 2(b)]. In the dark-field image [Fig. 2(c)], we observe distinct contrast at the outer corners of the matrix, although the low scattering contrast of Al introduces considerable noise. The fact that contrast can be found for the bulk Al despite the very low scattering power of bulk Al demonstrates the outstanding sensitivity of the grating interferometer for ultrasmall-angle scattering contributions. In the region of sharp edges refracted and nonrefracted contributions are superimposed and hence decrease the fringe visibility. This accounts for enhanced contrast in the reconstruction at corners and curves, i.e., wherever an edge is not well defined due to limited resolution. Figure 3(b) shows the first three-dimensional tomographic reconstruction based on neutron dark-field contrast. Because of the approach given in Eq. (2) standard tomography reconstruction algorithms can be used straightforwardly to recover the volumetric data displayed in Fig. 3(b). Additionally the new contrast mechanism for three-dimensional tomography introduced in this Letter helped to identify another feature of the investigated sample. In a few places sediments could be found. Figure 4 displays one of these regions of interest in a reconstructed cross section from phase contrast [Fig. 4(a)] as well as from dark-field contrast [Fig. 4(b)]. Because of the fact that the sediments are only up to 150 μm thick, they do not alter the shape of the surface considerably enough to be found in the reconstructed refractive index distribution. On the other hand considerable scattering from these structures enables the three-dimensional representation due to dark-field contrast displayed in Fig. 4(c).

These results are particularly important as they underline not only the high efficiency of the grating interferometer, but also the extremely high sensitivity to the effective local ultrasmall-angle scattering power. Additionally, the results demonstrate how the tomographic dark-field contrast approach can be applied even at low-brilliant sources such as state-of-the-art neutron sources. Generally, ultrasmall-angle-scattering–based reconstructions as derived from the dark-field images are particularly useful for identifying density variations due to structures in an object on the length scale of about a hundred nanometers to a few micrometers. This range naturally complements the

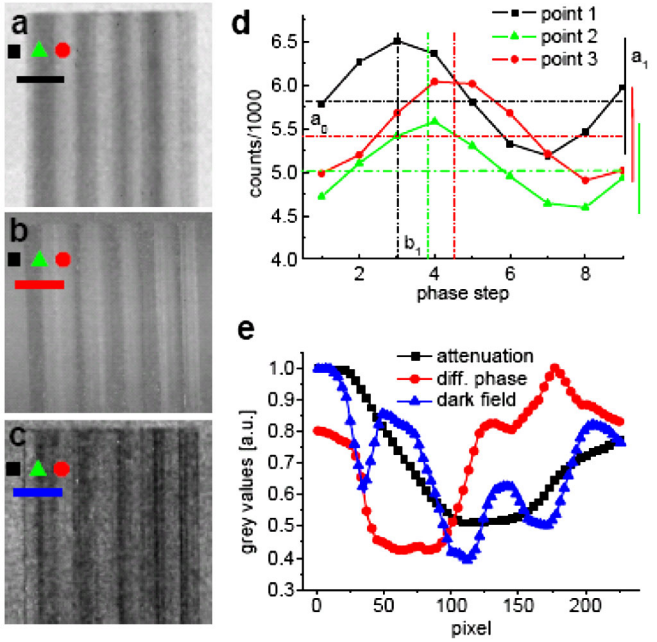

FIG. 2 (color online). Radiographic images: (a) attenuation, (b) differential phase (refraction), and (c) ultrasmall-angle scattering (dark-field image). (d) Attenuation parameter a_0 (offset), differential phase parameter b_1 (interferometer phase shift), and dark-field parameter basis a_1 (amplitude). (e) Line profiles corresponding to lines in (a–c).

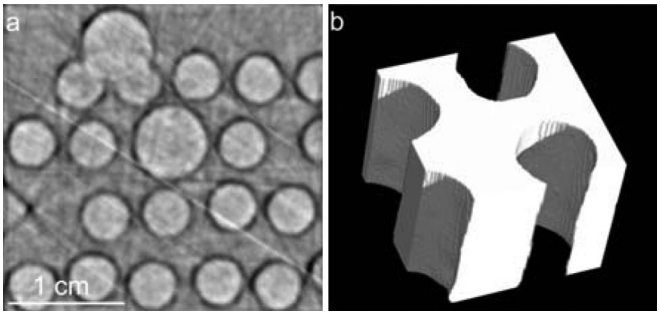

FIG. 3. Neutron dark-field tomography. (a) Reconstructed cross section from dark-field data of an Al matrix. (b) Representation of a detail of the volumetric reconstruction from dark-field data.

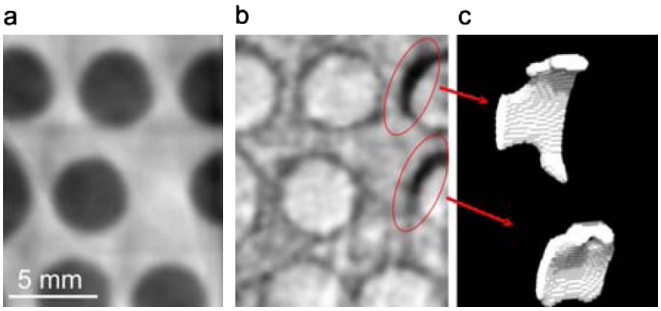

FIG. 4 (color online). Detail of tomographic reconstruction. (a) Phase contrast. (b) Dark-field contrast. (c) Isolated three-dimensional representation of the sediments found in the dark-field data.

size range spatially resolved directly by imaging methods. In conclusion we have shown how a grating interferometer can be used to produce dark-field tomographies with neutrons. We have demonstrated that in contrast to the existing crystal analyzer-based methods our new approach allows for three-dimensional dark-field computer tomography within practical time scales. Based on these results we conclude that this novel technique represents a major step forward not only for dark-field imaging with matter waves but also for the extension of dark-field imaging with x-rays to three dimensions. More generally the method is of particular interest because three contrast signals are measured simultaneously, maximizing the information content available from the sample. In summary the dark-field tomography approach with either neutrons or x-rays has clearly a high potential for a great number of applications.

We gratefully acknowledge the assistance of O. Ebrahimi in setting up the experiment. This work was partly supported by the BMBF Project No. 07TRTFH.

[1] A. Momose, Jpn. J. Appl. Phys. **44**, 6355 (2005).
[2] S. W. Wilkins, T. E. Gureyev, D. Gao, A. Pogany, and A. W. Stevenson, Nature (London) **384**, 335 (1996).
[3] K. A. Nugent, T. E. Gureyev, D. Cookson, D. Paganin, and Z. Barnea, Phys. Rev. Lett. **77**, 2961 (1996).
[4] M. Zawisky, U. Bonse, F. Dubus, Z. Hradil, and J. Rehacek, Europhys. Lett. **68**, 337 (2004).
[5] B. E. Allman, P. J. McMahon, K. A. Nugent, D. Paganin, D. L. Jacobson, M. Arif, and S. A. Werner, Nature (London) **408**, 158 (2000).
[6] P. J. McMahon, B. E. Allman, D. J. Jacobson, M. Arif, S. A. Werner, and K. A. Nugent, Phys. Rev. Lett. **91**, 145502 (2003).
[7] D. Chapman, W. Thomlinson, R. E. Johnston, E. Washburn, E. Pisano, N. Gmuer, Z. Zhong, R. Menk, F. Arfelli, and D. Sayers, Phys. Med. Biol. **42**, 2015 (1997).
[8] T. J. Davis, D. Gao, T. E. Gureyev, A. W. Stevenson, and A. W. Wilkins, Nature (London) **373**, 595 (1995).
[9] J. F. Clauser, U.S. Patent No. 5,812,629 (1998).
[10] F. Pfeiffer, T. Weitkamp, O. Bunk, and C. David, Nature Phys. **2**, 258 (2006).
[11] K. M. Podurets, V. A. Somenkov, and S. Sh. Shilstein, Physica B (Amsterdam) **156–157**, 691 (1989).
[12] W. Treimer, M. Strobl, A. Hilger, C. Seifert, and U. Feye-Treimer, Appl. Phys. Lett. **83**, 398 (2003).
[13] M. Strobl, W. Treimer, and A. Hilger, Nucl. Instrum. Methods Phys. Res., Sect. B **222**, 653 (2004).
[14] F. Pfeiffer, C. Gruenzweig, O. Bunk, G. Frei, E. Lehmann, and C. David, Phys. Rev. Lett. **96**, 215505 (2006).
[15] M. Strobl, W. Treimer, P. Walter, S. Keil, and I. Manke, Appl. Phys. Lett. **91**, 254104 (2007).
[16] G. R. Morrison and M. T. Browne, Rev. Sci. Instrum. **63**, 611 (1992).
[17] M. Ando, E. Hashimoto, H. Hashizume, K. Hyodo, H. Inoue, T. Kunisada, A. Maksimenko, K. Mori, E. Rubenstein, J. Roberson, D. Shimao, H. Sugiyama, K. Takeda, F. Toyofuku, E. Ueno, K. Umetani, H. Wada, and W. Pattanasiriwisawa, Nucl. Instrum. Methods Phys. Res., Sect. A **548**, 1 (2005).
[18] L. Rigon, H.-J. Besch, F. Arfelli, R.-H. Menk, G. Heitner, and H. Plothow-Besch, J. Phys. D **36**, A107 (2003).
[19] F. Pfeiffer, M. Bech, O. Bunk, P. Kraft, E. Eikenberry, Ch. Broennimann, C. Gruenzweig, and C. David, Nature Mater. **7**, 134 (2008).
[20] C. Grünzweig, C. David, O. Bunk, M. Dierolf, G. Frei, G. Kühne, J. Kohlbrecher, R. Schäfer, P. Lejcek, H. M. R. Rønnow, and F. Pfeiffer, Phys. Rev. Lett. (to be published).
[21] M. Strobl, W. Treimer, and A. Hilger, Appl. Phys. Lett. **85**, 488 (2004).
[22] J. D. Stephenson, M. P. Hentschel, and A. Lange, Nucl. Instrum. Methods Phys. Res., Sect. B **88**, 287 (1994).
[23] W. Treimer, M. Strobl, N. Kardjilov, A. Hilger, and I. Manke, Appl. Phys. Lett. **89**, 203504 (2006).
[24] N. Kardjilov, E. Lehmann, E. Steichele, and P. Vontobel, Nucl. Instrum. Methods Phys. Res., Sect. A **527**, 519 (2004).
[25] W. Kockelmann, G. Frei, E. H. Lehmann, P. Vontobel, and J. R. Santisteban, Nucl. Instrum. Methods Phys. Res., Sect. A **578**, 421 (2007);
[26] N. Kardjilov, I. Manke, M. Strobl, A. Hilger, W. Treimer, T. Krist, and M. Meissner, Nature Phys. **4**, 399 (2008).
[27] C. Grünzweig, F. Pfeiffer, O. Bunk, T. Donath, G. Kühne, G. Frei, M. Dierolf, and C. David, Rev. Sci. Instrum. **79**, 053703 (2008).
[28] Despite a wavelength resolution $\Delta\lambda/\lambda \sim 5\%$ (a factor of 6 better than necessary) the flux density was of the order of 10^5 cm^{-2} s^{-2} and hence still 2 orders of magnitude higher than in the only comparable measurements in a double crystal diffractometer [20]. Compared to the measurements in Ref. [21] the efficiency of our measurements was at least 8×10^2, i.e., nearly 3 orders of magnitude better.
[29] T. M. Sabine and W. K. Bertram, Acta Crystallogr. Sect. A **55**, 500 (1999).
[30] A. Hilger, N. Kardjilov, M. Strobl, W. Treimer, and J. Banhart, Physica B (Amsterdam) **385–386**, 1213 (2006).